

CONDENSED
MATTER

Phase Transformations in Nd–Fe–B-Based Alloys under High Pressure Torsion at Different Temperatures

B. B. Straumal^{a, b, c, d, *}, A. A. Mazilkin^{a, d}, S. G. Protasova^a, A. R. Kilmametov^{b, d},
A. V. Druzhinin^c, and B. Baretzky^d

^a Institute of Solid State Physics, Russian Academy of Sciences, Chernogolovka, Moscow region, 142432 Russia

^b Chernogolovka Scientific Center, Russian Academy of Sciences, Chernogolovka, Moscow region, 142432 Russia

^c National University of Science and Technology MISiS, Moscow, 119049 Russia

^d Institute of Nanotechnology, Karlsruhe Institute of Technology, Eggenstein-Leopoldshafen, 76344 Germany

*e-mail: straumal@issp.ac.ru

Received May 2, 2020; revised May 14, 2020; accepted May 14, 2020

In this work, we studied the behavior of the Nd–Dy–Fe–Co–Cu–B alloy for permanent magnets under high pressure torsion (HPT). In the initial state of the studied alloy, it mainly contained the crystalline phase τ_1 (Nd, Dy)₂(Fe, Co, Cu)₁₄B. After HPT at room temperature ($T_{\text{HPT}} = 30^\circ\text{C}$), a mixture of an amorphous phase with nanocrystalline inclusions of the τ_1 phase is observed in the alloy. In the equilibrium phase diagram, this state is equivalent to a mixture of the τ_1 phase with the melt at the temperature $T_{\text{eff}} = \sim 1100^\circ\text{C}$. The thus determined T_{eff} value is called the effective temperature. When the T_{HPT} temperature of the HPT treatment increases to 300 and 400°C, the amorphous phase disappears, and the Fe₂B and γ -Fe phases appear instead. In the equilibrium phase diagram, this state is equivalent to a mixture of phases $\tau_1 + \text{Fe}_2\text{B} + \gamma\text{-Fe}$, which is observed in the temperature range from ~ 950 to $\sim 1050^\circ\text{C}$. We explain this phenomenon by the fact that with an increase in the HPT temperature T_{HPT} , the rate of formation of defects during deformation remains constant, but the rate of their thermal relaxation (annihilation) increases. This is equivalent to decrease in the effective temperature T_{eff} in the equilibrium phase diagram. The previously predicted decrease in T_{eff} with an increase in T_{HPT} is observed for the first time.

DOI: 10.1134/S0021364020130020

During high-pressure torsion (HPT), a flat sample is placed between the rotating cemented carbide plungers to which external pressure is applied. Thus, the sample is located in a confined space and cannot be destroyed, and the HPT process can continue until the rotating hard plungers of the installation are destroyed. For soft metals and alloys (copper, aluminum), this means several hundreds of rotations [1–5]. For harder materials, such as Nd–Fe–B alloys, plungers withstand about 20 revolutions [6, 7]. What happens in the material in this process? Some idea gives us the magnitude of the rotation torque, which is measured during the test. It turns out that the torque quickly reaches saturation [5, 8–12]. This means that with the beginning of the process, a lot of defects (like vacancies, dislocations, grain boundaries) are formed in the sample, and then their concentration increases, which leads to hardening of the material. Along with the appearance of new defects, the process of their relaxation begins. In the case when the rate of appearance of new defects and the rate of their annihilation (relaxation) become equal, a stationary state (or steady

state) occurs [10, 13]. Not so long ago, it was found that this state is usually equifinal [10]. In other words, it does not depend on the structure and properties of the sample prior to straining [14–18]. For example, HPT leads to a sharp decrease in grain size (from a few millimeters to hundreds of nanometers). However, if the initial grain size is smaller than the stationary one, then the grains during HPT do not decrease, but grow [1, 19, 20]. The same thing happens, for example, with microhardness. Generally speaking, microhardness increases with HPT [2, 21, 22]. However, if its initial value is less than the stationary one, then the sample, on the contrary, is softened [23].

It is especially interesting to monitor phase transformations during HPT [16, 24–29]. They can tell a lot about the unusual stationary non-equilibrium state that occurs under such severe plastic deformation (SPD). These phase transformations include the decomposition and formation of a supersaturated solid solution upon dissolution of particles of the second phase [1, 16–18], transitions between allotropic modifications of materials [30–37], as well as amor-

phization of crystalline phases [38, 39] and crystallization of amorphous ones [38, 40, 41]. In the case of phase transformations, we also observe the equifinality. For example, the composition of the solid solution in two-phase systems at HPT is equifinal. If the initial composition c_{init} of solid solution was less than the stationary one c_{ss} , i.e., $c_{\text{init}} < c_{\text{ss}}$, then particles of the second phase dissolve in the volume and the concentration increases to c_{ss} . If the concentration in the solid solution before the HPT c_{init} was higher than c_{ss} ($c_{\text{init}} > c_{\text{ss}}$), on the contrary, new precipitates of the second phase are formed, and the concentration in the solid solution drops down to c_{ss} [16–18].

If we speak the language of the thermodynamics of irreversible processes [42–45], then the stationary state during HPT is sustainable, and is a certain attractor [42–45]. This means that if the initial state (structure and properties) of the material does not differ too much from the stationary one, then the system returns to the stationary state during the HPT and does not depend on the initial state. It is clear that in such a stationary state during HPT, the concentration of defects in the material is much higher compared to the equilibrium at the experiment temperature T_{HPT} . This means that the structure and properties of the phases formed during the HPT in the stationary state would differ from the structure and properties of the phase properties on the equilibrium phase diagrams for the conditions under which the HPT occurs. Usually, it is atmospheric pressure and room temperature. This means that in order to describe stationary states during HPT with a high concentration of defects, the special, nonequilibrium phase diagrams should exist [42–45]. Unfortunately, such diagrams are scarce or not studied at all. Therefore, in order to describe the phase transformations during HPT, we are forced to use the equilibrium phase diagrams. This approach was proposed by George Martin in order to describe the state of systems under severe neutron irradiation [46].

G. Martin showed back in 1984 that the phases that arose in a material after severe external action can be found on equilibrium phase diagrams [46]. As a rule, these phases in equilibrium phase diagrams are at a temperature above room temperature. This temperature was proposed to be called the effective temperature T_{eff} . Again, G. Martin also noted that this approach is suitable not only for crystalline, but also for amorphous phases. If the external influence is so strong that the concentration of defects exceeds some critical level, then the material is amorphized. Such a disappearance of the crystal structure can be considered as the equivalent of melting in the equilibrium phase diagram. It is intuitively clear that the effective temperature T_{eff} is related to the concentration of excess defects in the sample. The higher this concentration, the higher the effective temperature T_{eff} will be on the equilibrium phase diagram.

Thus, it was previously shown that the stationary state is equifinal and independent of the initial state of the sample [15–18]. However, it is clear that the stationary state is controlled by the dynamic equilibrium between the process of production of defects due to external deformation and the process of their annihilation (relaxation). Such relaxation (annihilation) usually occurs through barrier (thermally activated) mass transfer processes. It can be expected that if we increase the temperature of the HPT T_{HPT} above room temperature (by the heating of working part of the unit with an oven), then the rate of diffusion-controlled relaxation processes would increase, and the number of defects in a stationary state should decrease. Intuitively, the effective temperature T_{eff} should decrease as well. If, on the contrary, the experiment temperature T_{HPT} is lowered by cooling the working part of the HPT unit, then the equilibrium relaxation rate would decrease, and the stationary concentration of defects should increase. In this case, the configuration point on the equilibrium phase diagram should move upward, to a higher temperature T_{eff} and to a higher equilibrium concentration of defects.

The aim of this work was to find a direct experimental confirmation of our hypothesis that the effective temperature should decrease with increasing HPT temperature. For these experiments, we chose alloys based on the Nd–Fe–B system. Currently, such alloys serve as the basis for the best permanent magnets. We have previously observed that a mixture of crystalline phases in an Nd–Fe–B sample before HPT transforms after HPT into a mixture of amorphous and crystalline phases (or as a mixture of two amorphous phases) [6, 7]. This means that the respective configuration point on the equilibrium phase diagram is in the region where a mixture of two liquid phases or a mixture of melt and crystalline phases exists in equilibrium [6, 7]. In this work, we performed the HPT of such alloys at room and at elevated temperature.

The six-component Nd–Dy–Fe–Co–Cu–B alloy based on the Nd–Fe–B system was obtained from Vacuumschmelze GmbH (Germany). It was made using liquid phase sintering at a temperature of $\sim 1100^\circ\text{C}$, followed by annealing at $\sim 800^\circ\text{C}$ and a second, additional annealing at $\sim 550^\circ\text{C}$. It contained 66.5 wt % Fe, 22.1 wt % Nd, 9.4 wt % Dy, 1.0 wt % Co, 0.8 wt % B, 0.2 wt % Cu. The disks with a diameter of 10 mm and a thickness of 0.7 mm were cut from these samples by the electric spark erosion. The samples were subjected to HPT in a Bridgman anvil chamber (W. Klement GmbH, Lang, Austria) at a pressure of 7 GPa, 5 anvils rotations at a speed of 1 rpm, at room temperature, 300 and 400°C . For experiments at elevated temperatures, a special ring resistance furnace was used, placed around the anvils. Samples for structural studies were mechanically ground and polished on diamond paste with a grain size of up to 1 μm . Samples for scanning electron microscopy (SEM) were

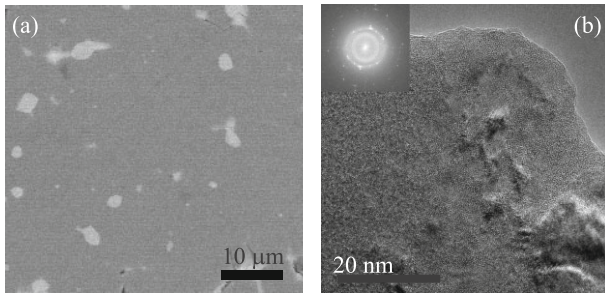


Fig. 1. (a) SEM image of the studied alloy before HPT. (b) Bright-field high-resolution TEM micrograph and FFT picture after HPT.

prepared by grinding, followed by polishing with anhydrous diamond emulsions to prevent excessive oxidation of the sample surface. Samples after HPT were cut out at a distance of 3 mm from the center of the deformed disk. The resulting sections were studied using scanning electron microscopy (SEM) and X-ray microanalysis on a Versa HighVac (FEI) instrument equipped with an EDAX energy dispersive spectrometer. X-ray diffraction patterns were obtained in the Bragg–Brentano geometry on a Bruker Discovery powder diffractometer using $\text{Co K}\alpha$ radiation. The lattice parameter was determined using the Fityk program [47]. The phases in the alloys were identified by comparison with ICSD phase bank data (FIZ Karlsruhe). Transmission electron microscopy (TEM) was performed on a TECNAI G2 FEG super TWIN (200 kV) microscope equipped with an EDAX energy dispersive spectrometer. Thin film samples for TEM were prepared on a PIPS device (Gatan Inc.). Magnetic properties were measured on a SQUID superconducting quantum interference device (Quantum-Design MPMS-7 and MPMS-XL).

Figure 1a shows a SEM micrograph of the studied Nd–Dy–Fe–Co–Cu–B alloy before HPT. In Fig. 1a, this alloy consists of coarse $\sim 30\text{-}\mu\text{m}$ grains of the “main” magnetic τ_1 phase $(\text{Nd, Dy})_2(\text{Fe, Co, Cu})_{14}\text{B}$ (it is dark-gray in the micrograph). In the triple junctions of these grains, the particles of the oxide phase of Nd_2O_3 rich in neodymium are visible, they look light-grey. Figure 1b shows a bright-field high-resolution TEM micrograph of the same alloy after HPT at 5 revolutions at room temperature. As can be seen from the micrograph and FFT (Fast Fourier Transform) picture, the sample mainly consists of an amorphous phase with small inclusions of crystalline particles $(\text{Nd, Dy})_2(\text{Fe, Co, Cu})_{14}\text{B}$.

In Fig. 2, the magnetization curves of the studied Nd–Dy–Fe–Co–Cu–B alloy before and after HPT at room temperature are shown. In the as-delivered state, the alloy studied has the excellent properties required for permanent magnets (saturation magnetization $J_s = 125 \text{ A m}^2 \text{ kg}^{-1}$, coercive force $H_c = 3.5 \text{ T}$). HPT almost completely transfers this alloy into the class of soft magnets: the coercive force H_c drops to $H_c = 1.5 \text{ T}$, and the saturation magnetization remains almost at the same level. The saturation magnetization indicates that the remaining crystalline phase is, apparently, the same τ_1 -phase $(\text{Nd, Dy})_2(\text{Fe, Co, Cu})_{14}\text{B}$.

Figure 3 shows the X-ray diffraction patterns of the studied Nd–Dy–Fe–Co–Cu–B alloy. In Fig. 3a the XRD pattern of this alloy in the as-delivered state is shown (i.e., after liquid phase sintering at $\sim 1100^\circ\text{C}$ and two additional anneals at $\sim 800^\circ\text{C}$ and $\sim 550^\circ\text{C}$). This pattern contains narrow peaks of the crystalline τ_1 -phase $\text{Nd}_2\text{Fe}_{14}\text{B}$ and small peaks of the oxide phase. The peaks of the τ_1 -phase are shifted to the high diffraction angles in comparison with the pure $\text{Nd}_2\text{Fe}_{14}\text{B}$ phase and correspond to the lattice constants of

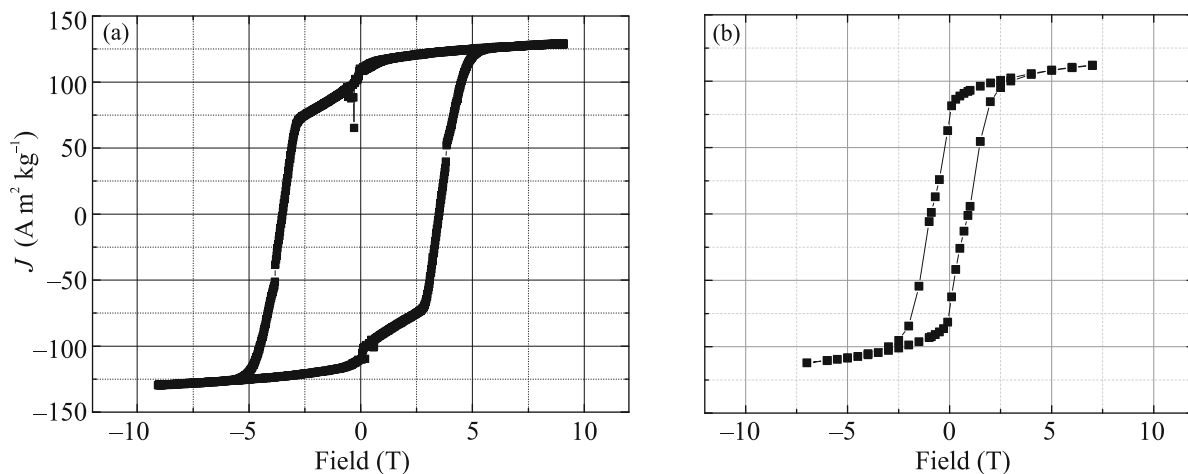


Fig. 2. Magnetization curves (a) before and (b) after HPT.

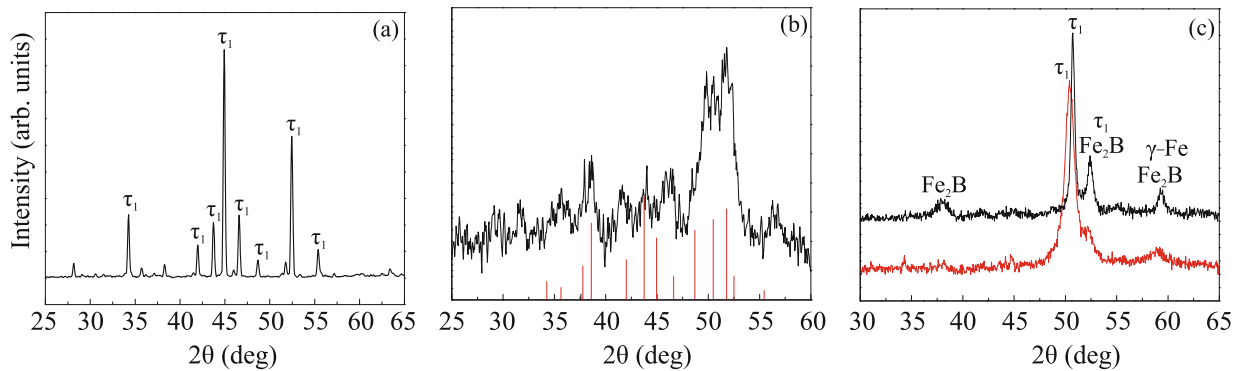


Fig. 3. (Color online) X-ray diffraction patterns. (a) Prior to HPT. Peaks of the τ_1 -phase are indicated. Small peaks correspond to the oxide phase of Nd_2O_3 . (b) After HPT at room temperature. Thin vertical lines mark the position of the peaks of the τ_1 -phase. (c) After HPT at (lower curve) 300 and (upper curve) 400°C. Peaks of the τ_1 , Fe_2B , and $\gamma\text{-Fe}$ phases are indicated.

$a = 0.87895$ nm and $c = 1.21460$ nm. Remember that our sample contains 22.1 wt % Nd and 9.4 wt % Dy. This means that only two thirds of the lattice sites of the τ_1 -phase are occupied by neodymium atoms, and the remaining third are occupied by dysprosium atoms. The lattice constants for $\text{Nd}_2\text{Fe}_{14}\text{B}$ are $a = 0.882$ nm, $c = 1.224$ nm, and for $\text{Dy}_2\text{Fe}_{14}\text{B}$ they are $a = 0.875$ nm, $c = 1.200$ nm [48]. This means that replacing some of the neodymium atoms with dysprosium ones reduces the lattice period of the τ_1 -phase, which we observe indeed in the pattern in Fig. 3a.

The XRD pattern in Fig. 3b corresponds to the sample after HPT at room temperature. The wide peak at about 52° also contains an amorphous halo, which is consistent with the results of TEM studies. Peaks in the spectrum are well explained by the set of overlapping peaks from the τ_1 -phase (their position is marked by thin vertical lines in Fig. 3b). The large width of the peaks is due to the fact that the particles of the τ_1 -phase remaining in the sample after HPT are very small (see TEM micrograph in Fig. 1b). An additional confirmation of the amorphization of the sample and the decrease in the amount of crystalline τ_1 -phase is a change in the magnetic properties (Fig. 2), namely, a decrease in the coercive force and a change in the saturation magnetization. The lower curve in Fig. 3c shows the XRD pattern after HPT at a temperature of 300°C. The amorphous halo almost disappeared, and fairly narrow peaks of the τ_1 -phase appear in the spectrum. In addition to them, peaks of the Fe_2B and $\gamma\text{-Fe}$ phases can be found in the pattern. Finally, the upper pattern in Fig. 3c corresponds to a sample subjected to HPT at 400°C. The halo of the amorphous phase is completely absent here, and the peaks of the crystalline τ_1 -phase, as well as the Fe_2B and $\gamma\text{-Fe}$ phases become narrow and sharp. The intensity of these peaks is noticeably higher in comparison

with the patterns of the samples subjected to HPT at room temperature and 300°C.

What is the reason for such an influence of the HPT temperature on the phase composition of the sample? Why do we see that the HPT of the initial sample containing only crystalline phases (mainly the τ_1 -phase) leads to almost complete amorphization of the material, as we observed earlier [6, 7]? An increase in the temperature of the HPT treatment leads to a decrease in the fraction of the amorphous phase after HPT at 300°C. After the HPT at 400°C, the amorphous phase completely disappears. We turn now to the diagram in Fig. 4. It shows the binary cross section of the ternary phase diagram for the Nd–Fe–B system at a constant iron concentration [49]. It should be noted that the studied alloy is actually six-component, however, multicomponent phase diagrams are poorly studied in this system. Therefore, the phase diagram for the three main components serves as a good approximation for our purposes, but it should be remembered that about a third of the neodymium atoms in the lattice of the τ_1 -phase are replaced by dysprosium atoms, and some of the iron atoms are replaced by cobalt and copper atoms. So, as we noted earlier [6, 7], HPT at room temperature leads to almost complete amorphization of the sample. Following the idea of G. Martin [46], we can find a point on the equilibrium phase diagram that approximately corresponds to this state, that is, a mixture of melt L with a certain amount of solid phase τ_1 . This point is indicated by a solid circle at a temperature of $T_{\text{eff}} \cong 1100^\circ\text{C}$. The HPT temperature $T_{\text{HPT}} = 30^\circ\text{C}$ for this sample is shown in the lower part of the diagram in an open circle.

With an increase in the HPT temperature to $T_{\text{HPT}} = 300^\circ\text{C}$, the amorphous phase practically disappears, and the crystalline phases τ_1 (mainly), Fe_2B , and $\gamma\text{-Fe}$ remain in the sample. A point equivalent to this state can be found in the phase diagram at a temperature of

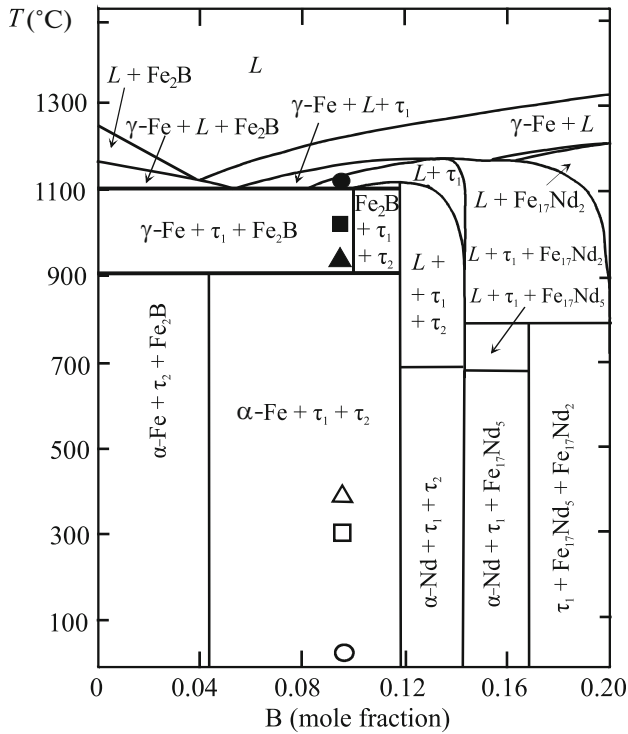


Fig. 4. Quasibinary cross-section of the Nd–Fe–B ternary phase diagram obtained by the Calphad method at a constant iron concentration of 80 at % [49]. The open symbols indicate the temperature of the HPT processing T_{HPT} , the solid symbols indicate the corresponding effective temperature T_{eff} .

$T_{eff} \cong 1000^\circ\text{C}$, where the liquid phase is absent. This state is shown in the phase diagram Fig. 4 by a solid square in the upper part of the region $\tau_1 + \text{Fe}_2\text{B} + \gamma\text{-Fe}$, near the melt formation temperature. The HPT temperature $T_{HPT} \cong 300^\circ\text{C}$ is shown by an open square in the lower part of Fig. 4. Finally, when the HPT temperature is $T_{HPT} = 400^\circ\text{C}$ (these HPT conditions are shown by an open triangle), the sample also contains only crystalline phases $\tau_1 + \text{Fe}_2\text{B} + \gamma\text{-Fe}$. This state is schematically marked in the diagram by a solid triangle at $T_{eff} \cong 950^\circ\text{C}$ in the lower part of the same field $\tau_1 + \text{Fe}_2\text{B} + \gamma\text{-Fe}$. In principle, the set of peaks in the curves of Fig. 3c can be interpreted also as a mixture of phases $\tau_1 + \text{Fe}_2\text{B} + \tau_2$. The τ_2 phase is $\text{Nd}_{4.5}\text{Fe}_{82.5}\text{B}_{12.5}$. In this case, the solid square and triangle in the phase diagram Fig. 4 would shift slightly to the right, from the region of $\tau_1 + \text{Fe}_2\text{B} + \gamma\text{-Fe}$ to the region of $\tau_1 + \text{Fe}_2\text{B} + \tau_2$. However, the set of peaks of the $\gamma\text{-Fe}$ phase is better for interpreting the spectra than those of τ_2 -phase, so we settled on the first option. In any case, T_{eff} for $T_{HPT} = 300$ and 400°C is above a temperature of 950°C , below which $\gamma\text{-Fe}$ is converted to $\alpha\text{-Fe}$. Thus, as follows from the diagram in Fig. 4,

an increase in the HPT temperature leads, as we expected, to a decrease in the effective temperature T_{eff} .

We previously found in the published results some indirect evidence of our idea of reducing T_{eff} with an increase in T_{HPT} [50]. For example, in [51], the HPT of TiNi shape memory alloys was studied. The authors deformed three titanium alloys with 48.5, 50, and 50.7 at % Ni at room temperature and at $T_{HPT} = 200, 250, 270,$ and 350°C . After deformation at $T_{HPT} = 30^\circ\text{C}$, both alloys were completely amorphous. In our language, this means that the effective temperature T_{eff} was above 1350°C , where only the liquid phase exists in this system [52]. With an increase in the HPT temperature to 200°C , a mixture of the amorphous phase and the NiTi intermetallic compound was observed in Ti–50.7 at % Ni and 270°C in Ti–48.5 at % Ni samples. This means that the configuration point for T_{eff} in the Ni–Ti phase diagram went down in temperature and ended up in the region where the melt and the NiTi phase coexist. For the Ti–48.5 at % Ni alloy, this corresponds to the temperature range $T_{eff} = 964\text{--}1310^\circ\text{C}$, and for the Ti–50.7 at % Ni alloy, to the range of $T_{eff} = 1250\text{--}1310^\circ\text{C}$ [52]. With a further increase in the T_{HPT} temperature of the HPT to 350°C , the amorphous phase did not appear in the samples [51]. They completely consisted of the nanocrystalline phase of a mixture of NiTi + Ti_2Ni phases for a Ti–48.5 at % Ni alloy and NiTi + TiNi_2 for a Ti–50.7 at % Ni alloy. This means that the effective temperature T_{eff} dropped even lower to the region of coexistence of the NiTi + Ti_2Ni or NiTi + TiNi_2 phases in the phase diagram, that is, below 984 and 1118°C , respectively [52].

We use the concept of effective temperature T_{eff} to emphasize that in our work we are talking about phase transformations under conditions far from equilibrium. Namely: phase transformations during high pressure torsion occur under conditions when external deformation produces a huge number of defects, and they, in turn, continuously relax (annihilate), and as a result, a state of dynamic equilibrium arises.

There is a certain similarity between our experiments and experiments on solid-phase amorphization under high pressure in the conditions close to equilibrium (that is, simply by applying external pressure without simultaneous severe deformation) [53–58]. Indeed, in our case, with an increase in the temperature of the HPT experiment T_{HPT} , the amorphous phase disappears. This is because in a stationary state, the diffusion relaxation of defects caused by external deformations accelerates with increasing T_{HPT} . Near equilibrium, the solid-state amorphization is observed both upon application of pressure and upon its removal. For example, ice is amorphized under compression at temperatures below 130 K, and at higher

temperatures, it crystallizes into high-pressure phases [53–55]. Conversely, in other cases, the high-pressure phase occurs during compression, and when the pressure is relieved, it cannot turn into low-pressure phases due to the slow mass transfer [56–58]. However, with an increase in the experimental temperature, such a high-pressure phase does not amorphize, and manages to turn into low-pressure phases [56–58].

However, this similarity is misleading. In experiments [53–58], an increase in temperature actually accelerates diffusion mass transfer and leads to the transformation of the amorphous phase into a crystalline one. The usual equilibrium phase diagrams are quite suitable for describing these experiments. In our case, the system is far from equilibrium, and the stationary concentration of defects during HPT is constantly increased (compared to equilibrium with T_{HPT}). Generally speaking, one needs the non-equilibrium phase diagrams to describe this state. However, such diagrams are absent, and using equilibrium diagrams, we agree that we are not talking about the “real,” but about the effective temperature T_{eff} .

Of course, the definition of T_{eff} under conditions when in one case we have an amorphous phase and in the other it is absent is not very impressive. Fortunately, there are cases when the effective temperature can be determined with a high accuracy of $\pm 10\text{--}20^\circ\text{C}$, if the phase composition continuously changes over a wide range of concentration and temperature, such as in the case of competition between the formation and decomposition of a solid solution in binary systems [15]. In this case, such a phase transformation is described on the phase diagram by the continuous solvus curve (i.e., the temperature dependence of the solubility of the second component in the solid solution). This solubility can vary over a wide range of concentration and temperature. In this case, by determining the stationary concentration of the second component in the solid solution after HPT, we can estimate the T_{eff} value with high accuracy.

We previously observed that HPT causes accelerated mass transfer [15, 16, 18, 59, 60]. In this case, we estimated the equivalent diffusion coefficient, for example, in the case of the HPT-induced competition between the decomposition of a solid solution and the dissolution of particles in copper alloys [15, 18, 59, 60]. Let us make a similar estimation for mixing in an alloy based on the Nd–Fe–B system. For such an estimation, it is necessary that the phases before and after the HPT differ in composition. In our case, before the HPT, the sample contained only the τ_1 -phase (Fig. 3a), and after the HPT at $T_{\text{HPT}} = 300^\circ\text{C}$, γ -Fe appears in the sample in addition to the τ_1 -phase (Fig. 3c). The characteristic size of crystalline particles after HPT is about 20 nm (Fig. 1b). The time required to achieve this stationary state is approxi-

mately $t = 350$ s. Using the simple formula $L = (Dt)^{0.5}$ for mass transfer by the volume diffusion, we obtain the estimate $D = 10^{-18} \text{ m}^2 \text{ s}^{-1}$ for the bulk diffusion coefficient necessary for the formation of γ -Fe particles. Extrapolation of the data on volume self-diffusion in γ -Fe to the HPT temperature $T_{\text{HPT}} = 300^\circ\text{C}$ gives $D = 10^{-28} \text{ m}^2 \text{ s}^{-1}$ [61–64], and for self-diffusion in α -Fe, $D = 10^{-30} \text{ m}^2 \text{ s}^{-1}$ [63–68]. Thus, under the influence of HPT in the studied Nd–Dy–Fe–Co–Cu–B alloy, accelerated mass transfer occurs at a rate of 10–12 orders of magnitude higher than the rate of ordinary thermal diffusion at $T_{\text{HPT}} = 300^\circ\text{C}$, and this despite the fact that high pressure itself significantly reduces the kinetic mass transfer coefficients [69, 70].

Volume diffusion with the coefficient $D = 10^{-18} \text{ m}^2 \text{ s}^{-1}$ occurs in the γ -iron at $\sim 900^\circ\text{C}$ [61–64]. This temperature is quite comparable with the value $T_{\text{eff}} \cong 950\text{--}1000^\circ\text{C}$, determined above by the presence of phases in the phase diagram (Fig. 4). Accelerated mass transfer, most likely, is explained by an increased concentration of defects (in particular, vacancies) during HPT, and this, in turn, is equivalent to an increase in temperature from T_{HPT} to T_{eff} . It is clear that, in fact, in the case of HPT, there is no real increase in temperature or acceleration of diffusion [26, 28, 29, 33, 59, 71]. It is just that in case of HPT we are dealing with mass transfer over distances much larger than interatomic ones. In this case, many defects of various types arise (and disappear). As a result, the final picture of processes during HPT is similar to that observed with increasing temperature [72–75].

Thus, our experiments are a direct confirmation of the hypothesis of a decrease in T_{eff} with an increase in T_{HPT} , expressed at the beginning of this article. In other words, if the deformation conditions remain unchanged (and in our case this is the anvil shape, applied pressure, strain rate, and number of revolutions), then the phase composition of the sample is controlled by the experiment temperature T_{HPT} . The presence of certain phases in the sample during HPT is determined by the equilibrium between the rate of defects production under the influence of external forces and the rate of their annihilation (relaxation) by the diffusion-controlled mass transfer. With increasing temperature of the experiment T_{HPT} , the rate of defects production remains constant, and the rate of their relaxation increases. This means that the stationary concentration of defects should decrease. Using an equilibrium phase diagram as a tool, we see that the phase composition of the sample after HPT can be found in the diagram at ever lower temperatures T_{eff} . It seems to us that such a shift just means that the stationary concentration of defects in the sample decreases with increasing temperature of the experi-

ment T_{HPT} . Thus, in this work, for the first time, we obtained direct experimental confirmation of the hypothesis of a stationary defect concentration during HPT and its dependence on the experimental temperature.

ACKNOWLEDGMENTS

We are grateful to Vacuumschmelze GmbH (Dr. M. Katter) for the alloys provided for research.

FUNDING

This work was partially carried out within the framework of the state assignment of the Institute of Solid State Physics (ISSP) and the Chernogolovka Scientific Center, Russian Academy of Sciences, with the support of the Scientific Facility Center at the ISSP, as well as with the financial assistance of the Russian Foundation for Basic Research (project nos. 18-33-00473, 19-33-90125, and 19-58-06002) and the Industrielle Gemeinschaftsforschung Foundation (Germany, grant no. 19838N).

REFERENCES

1. C. Borchers, C. Garve, M. Tiegel, M. Deutges, A. Herz, K. Edalati, R. Pippan, Z. Horita, and R. Kirchheim, *Acta Mater.* **97**, 207 (2015).
2. S. Lee and Z. Horita, *Mater. Trans.* **53**, 38 (2012).
3. K. Edalati, S. Toh, M. Watanabe, and Z. Horita, *Scr. Mater.* **66**, 386 (2012).
4. J. M. Cubero-Sesin and Z. Horita, *Mater. Trans.* **53**, 46 (2012).
5. K. Bryla, J. Morgiel, M. Faryna, K. Edalati, and Z. Horita, *Mater. Lett.* **212**, 323 (2018).
6. B. B. Straumal, A. R. Kilmametov, A. A. Mazilkin, S. G. Protasova, K. I. Kolesnikova, P. B. Straumal, and B. Baretzky, *Mater. Lett.* **145**, 63 (2015).
7. B. B. Straumal, A. A. Mazilkin, S. G. Protasova, D. V. Gunderov, G. A. López, and B. Baretzky, *Mater. Lett.* **161**, 735 (2015).
8. B. B. Straumal, A. R. Kilmametov, A. A. Mazilkin, A. S. Gornakova, O. B. Fabrichnaya, M. J. Kriegel, D. Rafaja, M. F. Bulatov, A. N. Nekrasov, and B. Baretzky, *JETP Lett.* **111**, 624 (2020).
9. B. B. Straumal, A. A. Mazilkin, B. Baretzky, E. Rabkin, and R. Z. Valiev, *Mater. Trans.* **53**, 63 (2012).
10. B. B. Straumal, A. R. Kilmametov, Yu. Ivanisenko, A. A. Mazilkin, O. A. Kogtenkova, L. Kurmanaeva, A. Korneva, P. Zieba, and B. Baretzky, *Int. J. Mater. Res.* **106**, 657 (2015).
11. K. Edalati, D. J. Lee, T. Nagaoka, M. Arita, H. S. Kim, Z. Horita, and R. Pippan, *Mater. Trans.* **57**, 533 (2016).
12. K. Edalati, Z. Horita, T. Furuta, and S. Kuramoto, *Mater. Sci. Eng. A* **559**, 506 (2013).
13. K. Edalati and Z. Horita, *Acta Mater.* **59**, 6831 (2011).
14. L. von Bertalanffy, *Science* (Washington, DC, U. S.) **111**, 23 (1950).
15. B. B. Straumal, A. R. Kilmametov, A. Korneva, A. A. Mazilkin, P. B. Straumal, P. Zieba, and B. Baretzky, *J. Alloys Compd.* **707**, 20 (2017).
16. B. B. Straumal, B. Baretzky, A. A. Mazilkin, F. Philipp, O. A. Kogtenkova, M. N. Volkov, and R. Z. Valiev, *Acta Mater.* **52**, 4469 (2004).
17. B. B. Straumal, S. G. Protasova, A. A. Mazilkin, E. Rabkin, D. Goll, G. Schütz, B. Baretzky, and R. Valiev, *J. Mater. Sci.* **47**, 360 (2012).
18. B. Straumal, A. R. Kilmametov, Yu. O. Kucheev, L. Kurmanaeva, Yu. Ivanisenko, B. Baretzky, A. Korneva, P. Zieba, and D. A. Molodov, *Mater. Lett.* **118**, 111 (2014).
19. X. Z. Liao, A. R. Kilmametov, R. Z. Valiev, H. Gao, X. Li, A. K. Mukherjee, J. F. Bingert, and Y. T. Zhu, *Appl. Phys. Lett.* **88**, 021909 (2006).
20. H. Wen, R. K. Islamgaliev, K. M. Nesterov, R. Z. Valiev, and E. J. Lavernia, *Philos. Mag. Lett.* **93**, 481 (2013).
21. K. Edalati, Y. Hashiguchi, P. H. R. Pereira, Z. Horita, and T. G. Langdon, *Mater. Sci. Eng. A* **714**, 167 (2018).
22. M. Y. Alawadhi, S. Sabbaghianrad, Y. Huang, and T. G. Langdon, *J. Mater. Res. Technol.* **6**, 369 (2017).
23. A. A. Mazilkin, B. B. Straumal, M. V. Borodachenkova, R. Z. Valiev, O. A. Kogtenkova, and B. Baretzky, *Mater. Lett.* **84**, 63 (2012).
24. S. K. Pabi, J. Joardar, and B. S. Murty, *Proc. Ind. Natl. Sci. Acad. A* **67**, 1 (2001).
25. X. Sauvage, A. Chbihi, and X. Queleennec, *J. Phys.: Conf. Ser.* **240**, 012003 (2010).
26. V. I. Levitas and O. M. Zarechnyy, *Phys. Rev. B* **82**, 174123 (2010).
27. B. B. Straumal, A. R. Kilmametov, Yu. Ivanisenko, A. A. Mazilkin, O. A. Kogtenkova, L. Kurmanaeva, A. Korneva, P. Zieba, and B. Baretzky, *Int. J. Mater. Res.* **106**, 657 (2015).
28. M. Javanbakht and V. I. Levitas, *Phys. Rev. B* **94**, 214104 (2016).
29. V. I. Levitas, *Mater. Trans.* **60**, 1294 (2019).
30. B. B. Straumal, A. A. Mazilkin, B. Baretzky, E. Rabkin, and R. Z. Valiev, *Mater. Trans.* **53**, 63 (2012).
31. Y. Ivanisenko, I. MacLaren, X. Sauvage, R. Z. Valiev, and H.-J. Fecht, *Acta Mater.* **54**, 1659 (2006).
32. M. T. Pérez-Prado and A. P. Zhilyaev, *Phys. Rev. Lett.* **102**, 175504 (2009).
33. B. Feng and V. I. Levitas, *Mater. Sci. Eng. A* **680**, 130 (2017).
34. K. Edalati, E. Matsubara, and Z. Horita, *Metall. Mater. Trans. A* **40**, 2079 (2009).
35. B. Feng, V. I. Levitas, and M. Kamrani, *Mater. Sci. Eng. A* **731**, 623 (2018).
36. Y. Ivanisenko, A. Kilmametov, H. Roesner, and R. Valiev, *Int. J. Mater. Res.* **99**, 36 (2008).
37. B. Feng, V. I. Levitas, and W. Li, *Int. J. Plastic.* **113**, 236 (2019).
38. V. I. Levitas, *Phys. Rev. Lett.* **95**, 075701 (2005).
39. V. I. Levitas, Y. Ma, E. Selvi, J. Wu, and J. A. Patten, *Phys. Rev. B* **85**, 054114 (2012).

40. A. M. Glezer, M. R. Plotnikova, A. V. Shalimova, and S. V. Dobatkin, *Bull. Russ. Acad. Sci. Phys.* **73**, 1233 (2009).
41. S. Hóbor, Á. Révész, A. P. Zhilyaev, and Zs. Kovacs, *Rev. Adv. Mater. Sci.* **18**, 590 (2008).
42. I. Prigogine, *Introduction to Thermodynamics of Irreversible Processes* (Wiley, New York, London, 1955).
43. G. Nikolis and I. Prigogine, *Self-Organization in Non-Equilibrium Systems* (Wiley, New York, London, 1977).
44. D. Kondepudi and I. Prigogine, *Modern Thermodynamics. From Heat Engine to Dissipative Structures*, 2nd ed. (Wiley, Chichester, UK, 2015).
45. I. Prigogine and I. Stengers, *Order out of Chaos. Man's New Dialog with Nature* (Verso, London, New York, 2017).
46. G. Martin, *Phys. Rev. B* **30**, 1424 (1984).
47. M. Wojdyr, *J. Appl. Crystallogr.* **43**, 1126 (2010).
48. M. Sagawa, S. Fujimura, H. Yamamoto, Y. Matsuura, and K. Hiraga, *IEEE Trans. Magn.* **20**, 1584 (1984).
49. T. L. Chen, J. Wang, C. P. Guo, R. Li, Z. M. Du, G. H. Rao, and H. Y. Zhou, *Calphad* **66**, 101627 (2019).
50. B. Straumal, A. Korneva, and P. Zieba, *Arch. Civil Mech. Eng.* **14**, 242 (2014).
51. S. D. Prokoshkin, I. Yu. Khmelevskaya, S. V. Dobatkin, I. B. Trubitsyna, E. V. Tatyatin, V. V. Stolyarov, and E. A. Prokofiev, *Acta Mater.* **53**, 2703 (2005).
52. *Binary Alloy Phase Diagrams*, Ed. by T. B. Massalski, 2nd ed. (ASM Int., Materials Park, OH, 1990).
53. E. L. Gromnitskaya, O. V. Stal'gorova, A. G. Lyapin, V. V. Brazhkin, and O. B. Tarutin, *JETP Lett.* **78**, 488 (2003).
54. E. L. Gromnitskaya, A. G. Lyapin, O. V. Stal'gorova, I. V. Danilov, and V. V. Brazhkin, *JETP Lett.* **96**, 789 (2012).
55. E. L. Gromnitskaya, O. V. Stal'gorova, and V. V. Brazhkin, *J. Exp. Theor. Phys.* **112**, 109 (1997).
56. V. V. Brazhkin, A. G. Lyapin, S. V. Popova, and R. N. Voloshin, *JETP Lett.* **56**, 152 (1992).
57. O. I. Barkalov, I. T. Belash, and E. G. Ponyatovsky, *High Press. Res.* **4**, 390 (1990).
58. V. E. Antonov, A. E. Arakelyan, O. I. Barkalov, A. F. Gurov, E. G. Ponyatovsky, V. I. Rashupkin, and V. M. Teplinsky, *J. Alloys Compd.* **194**, 279 (1993).
59. B. B. Straumal, V. Pontikis, A. R. Kilmametov, A. A. Mazilkin, S. V. Dobatkin, and B. Baretzky, *Acta Mater.* **122**, 60 (2017).
60. B. B. Straumal, A. R. Kilmametov, I. A. Mazilkin, A. Korneva, P. Zieba, and B. Baretzky, *JETP Lett.* **110**, 624 (2019).
61. I. G. Ivantsov and A. M. Blinkin, *Fiz. Met. Metalloved.* **22**, 876 (1966).
62. Th. Heumann and R. Imm, *J. Phys. Chem. Solids* **29**, 1613 (1968).
63. C. M. Walter and N. L. Peterson, *Phys. Rev.* **178**, 922 (1968).
64. D. Graham, *J. Appl. Phys.* **40**, 2386 (1969).
65. R. J. Borg and C. E. Birchenall, *Trans. Metall. Soc. AIME* **218**, 980 (1960).
66. G. Hettich, H. Mehrer, and K. Maier, *Scr. Metall.* **11**, 795 (1977).
67. J. Geise and C. Herzig, *Z. Metallkd.* **78**, 291 (1987).
68. H. Mehrer and M. Ltibehusen, *Def. Dif. Forum* **66–69**, 591 (1989).
69. B. B. Straumal, L. M. Klinger, and L. S. Shvindlerman, *Scr. Metall.* **17**, 275 (1983).
70. D. A. Molodov, B. B. Straumal, and L. S. Shvindlerman, *Scr. Metall.* **18**, 207 (1984).
71. B. B. Straumal, A. R. Kilmametov, G. A. López, I. López-Ferreño, M. L. Nó, J. San Juan, H. Hahn, and B. Baretzky, *Acta Mater.* **125**, 274 (2017).
72. T. Kim, G. Ouyang, J. D. Poplawsky, M. J. Kramer, V. I. Levitas, J. Cui, and L. Zhou, *J. Alloys Compd.* **808**, 151743 (2019).
73. M. Kamrani, V. I. Levitas, and B. Feng, *Mater. Sci. Eng. A* **705**, 219 (2017).
74. V. I. Levitas and A. M. Roy, *Phys. Rev. B* **91**, 174109 (2015).
75. V. I. Levitas, *Int. J. Plastic.* **106**, 164 (2018).